JOURNAL OF CATALYSIS 93, 100–121 (1985)

Catalytic Hydrodemetallation of Nickel Porphyrins

I. Porphyrin Structure and Reactivity

ROBERT A. WARE[1] AND JAMES WEI[2]

Department of Chemical Engineering, Massachusetts Institute of Technology, Cambridge, Massachusetts 02139

Received March 29, 1984; revised November 27, 1984

The kinetics and mechanism of hydrodemetallation reactions and the pattern of metal deposition have been investigated using a model residuum oil, consisting of nickel porphyrins (Ni-etioporphyrin, Ni-tetraphenylporphyrin, and Ni-tetra(3-methylphenyl)porphyrin) dissolved in a mineral oil and reacted over an unsulfided $CoMo/Al_2O_3$ catalyst at 285–345°C and 4.58–10.09 MPa H_2 (650–1450 psig). The porphyrins react via a sequential mechanism, first involving hydrogenation of peripheral double bonds, followed by the final hydrogenolysis step which fragments the ring and removes the metal. Porphyrin molecular structure exerts, through chemical and steric effects, an impact on this reaction pathway. For Ni-etioporphyrin, there is one hydrogenated reaction intermediate and the rate-limiting step is initial hydrogenation. For Ni-tetra(3-methylphenyl)porphyrin, there are three reaction intermediates and the rate-limiting step is final hydrogenolysis and ring opening. Temperature and hydrogen pressure dependencies of the kinetic parameters have been determined. The rate constants are invariant of nickel concentrations from 16 to 90 ppm. Nickel-deposition profiles generated under diffusion-limited conditions in 1.5-mm extrudates have been successfully modeled using intrinsic kinetic parameters obtained with crushed catalysts and diffusivities on the order of 10^{-6} cm²/sec.

1. INTRODUCTION

Nickel and vanadium, the principal metals in petroleum oil, are present in structures such as porphyrins and the more condensed asphaltenes in concentrations ranging up to 1300 ppm by weight Ni and V (*1*). During catalytic hydroprocessing for sulfur and nitrogen removal, these metal-bearing molecules undergo hydrodemetallation (HDM) reactions leading to metal deposition and catalyst poisoning. Deactivation occurs by direct fouling of active sites and by physical obstruction of the entrance to the fine pores. Many metal-bearing species and other heteroatom species in the resid undergo complicated and competing catalytic reactions. The use of model compounds eliminates many of these difficulties, enabling a clearer picture of the inherent reactions to be obtained.

Hung (*2*) in his pioneering model compound work with metallo-porphyrins observed fractional kinetic order in total metal removal rates. These were interpreted by Agrawal (*3*) to be the result of a sequential HDM mechanism. The metal deposition occurred from a hydrogenated intermediate not originally in the oil. This mechanism explains the reactor axial position dependence of metal-deposition profiles obtained from hydrotreating reactors with model heavy oils (*3*) and industrial feedstocks (*4*).

More recently, Rankel (*5*) and Kameyama and Amano (*6*) have investigated the catalytic reaction pathways of Ni- and VO-petroporphyrins with model compounds. Their work qualitatively confirms the sequential nature of HDM reactions proposed by Agrawal (*3*).

This paper examines in detail the HDM

[1] Present address: Mobil Research and Development Corp., Paulsboro, N.J. 08066.

[2] To whom correspondence should be addressed.

0021-9517/85 $3.00

mechanism of three nickel porphyrins. The influence of molecular structure in determining the reaction pathway and the overall rate-limiting step for metal removal are demonstrated. This information is important when attempting to interpret and to predict the pattern of metal deposition in industrial hydroprocessing catalysts.

2. EXPERIMENTAL

A model oil system consisting of well-characterized Ni-porphyrins dissolved in a clean mineral oil has been used in this investigation to simulate high metal residuum. The three Ni-porphyrins used are shown in Fig. 1, and were purchased from Midcentury Chemicals (Posen, Ill.). Ni-Etio (Ni-EP)-type porphyrins have been identified in crude oil comprising up to 50% of the metal in the free-porphyrin fraction (*7*). Ni-tetraphenylporphyrin (Ni-TPP), although not identified in oil, may be representative of bound porphyrins of higher aromaticity existing in the petroleum asphaltenes (*8*). The use of Ni-TPP was limited, however, due to its low solubility of 20 ppm Ni in the mineral oil. A derivative of Ni-TPP, namely Ni-tetra(3-methylphenyl)porphyrin (Ni-T3MPP), exhibited much greater solubility in the oil (up to 120 ppm Ni). The procedure for dissolving these porphyrins in the mineral oil has been described by Agrawal (*3*).

The mineral oil solvent was a white oil marketed under the name Nujol. Nujol is a mixture of saturated hydrocarbons consisting primarily of naphthenes. It was free of sulfur and nitrogen compounds and was essentially inert at reaction conditions (*3*).

A commercial $CoO–MoO_3/\gamma\text{-}Al_2O_3$ hydrodesulfurization catalyst (American Cyanamid, HDS-16A) was used as the principal catalyst in this investigation. The composition and properties of the catalyst, supplied as 1/16-in. extrudates, are listed in Table 1. Kinetic results were obtained on crushed 170–200 mesh (0.074–0.088 mm diam.) catalyst particles which have been shown to be free of diffusional limitations. A second set of runs conducted under diffusion-limited conditions, with the 1/16-in. catalyst extrudates, yielded measurement of intrapellet nickel-deposition profiles. All results reported are on the unsulfided catalyst. While not representative of industrial "working" catalysts, the oxide form provides a clean environment to study the reactions. Recognizing the importance of the sulfided catalyst and the difference in active sites on the oxide and sulfide forms, the sulfided catalyst is examined in Part II (*24*).

TABLE 1

Catalyst Composition and Properties

$CoO–MoO_3/\gamma\text{-}Al_2O_3$, HDS-16A American Cyanamid	
CoO:	5.7 wt%
MoO_3:	12.2 wt%
Average pore diameter:	80.4 Å
Surface area:	176 m^2/g
Pore volume:	0.43 ml/g

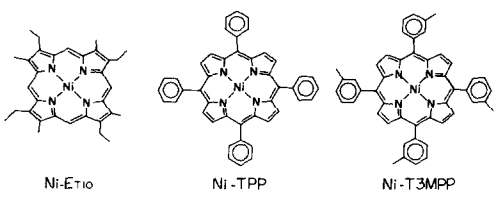

FIG. 1. Structure of model nickel compounds.

All experiments were performed in a high-pressure and high-temperature packed-bed reactor. A full description of the apparatus has been given by Agrawal (*3*). The reactor operated in an upflow mode with no gas phase present. All hydrogen required for reaction was supplied by the oil which was first saturated at room temperature with hydrogen (99.999% purity, Matheson Gas Products). Calculations demonstrated that the solubility of hydrogen in the oil was far in excess of that required for complete porphyrin saturation (100–200 mole hydrogen/mole porphyrin) under reaction conditions. Operating conditions ranged from 285 to 345°C at hydrogen pressures of 4.58–10.09 MPa H_2 (650–1450

psig) and contact times, W/Q, of 0.007 to 0.7 g cat. hr/ml oil (LHSV = 1.35–135 hr^{-1}). All kinetic results reported are for catalyst batches aged a minimum of 80 hr so that transients in catalytic activity reported by Agrawal (*3*) have been minimized. Catalyst charges were on stream for as long as 350 hr. At the low metal loadings attained in these experiments (generally less than 2 wt% Ni) no significant catalyst deactivation due to pore plugging was observed.

3. ANALYTICAL

Effluent oil samples were subjected to analysis by several techniques. Atomic absorption spectrophotometry (Perkin–Elmer 360) was used to determine the total Ni concentration. Ultraviolet–visible spectrophotometry (Bausch & Lomb Spectronic 2000) was used in conjunction with Beer's law to determine the concentration of the individual porphyrinic species. Liquid chromatography proved useful in isolating and identifying reaction intermediates and products. Two systems were developed; a 3.9 mm × 30-cm μPorasil column (Waters Associates) with a mobile phase of hexane/1,2-dimethoxyethane (100/1) for Ni-Etio samples and a 3.9 mm × 30-cm μBondapak-CN column (Waters Associates) with hexane/ethanol (400/1) as the mobile phase for Ni-T3MPP samples. Dual-wavelength detection at 254 and 405 nm provided differentiation between the porphyrinic and nonporphyrinic peaks. A rapid scanning uv–visible spectrophotometer (Hewlett–Packard 8450A) was also used in conjunction with the LC analysis. This provided complete spectra of individual peaks as they eluted from the column.

Key intermediates in the demetallation of Ni-T3MPP were concentrated by repetitive sample injection and peak collection off the LC to obtain sufficient quantities to enable further characterization. Mass spectroscopy was performed by Skinner and Sherman Laboratories, Inc. (Waltham, Mass.) by solid-probe chemical ionization using ammonia as the ionizing source. Solution infrared spectroscopy was performed using a Nicolet 7000 Series FTIR operated at 4-cm^{-1} resolution with tetrachloroethylene as the reference solvent.

Radial nickel profiles in the 1/16-in. pellets were obtained using an electron microprobe (Applied Research Laboratories Model EMX/SM). The catalyst pellets examined were carefully removed from specified positions along the reactor length, washed in a Soxhlet extractor for 24 hr with xylene, and dried overnight in an oven. The pellets were then mounted in an epoxy resin and ground down so that the cross section at midlength was exposed. The final surface polishing was done with 3-μm diamond abrasive paper.

4. KINETIC RESULTS

a. Ni-Etio

Hydrodemetallation kinetics for Ni-Etio on the oxide form of $CoMo/Al_2O_3$ were first reported by Agrawal (*3*) to proceed via a sequential mechanism. The first step involved reversible hydrogenation of a peripheral double bond in one of the four pyrrole rings comprising the macrocycle to form the Ni-etiochlorin ($Ni\text{-}EPH_2$) as shown in Fig. 2. The $Ni\text{-}EPH_2$ then reacted via a hydrogenolysis step which fragmented the ring and deposited the metal on the catalyst. With Ni-Etio, the visible spectra of effluent oil shown in Fig. 3 only reveals absorption peaks for Ni-EP and $Ni\text{-}EPH_2$. These are assigned based on pure-component spectra previously reported (*14, 29*) and also shown in Fig. 4 from HPLC analysis of effluent oil. The HPLC analysis of oil samples also indicated few intermediates. One other major peak in addition to the Ni-EP and $Ni\text{-}EPH_2$ species was detected with

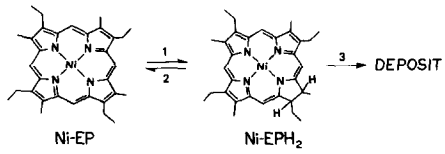

FIG. 2. Reaction sequence for Ni-etioporphyrin.

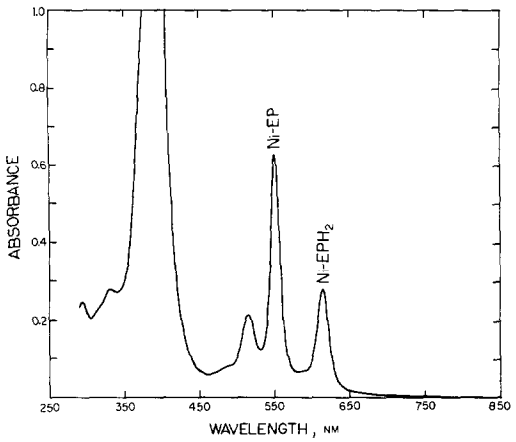

FIG. 3. Absorption spectra of effluent oil sample during HDM of Ni-etioporphyrin at 317°C and 6.99 MPa H_2 (1000 psig); background is xylene.

a retention time similar to pyrrole and no absorption bands above 290 nm in its spectra. This third component is presumably the fragmented remains of the ring once the metal has been removed. No metal-free porphyrinic rings are detected in the effluent oil. Experiments by Hung (*2*) using free-base etioporphyrin as the feed have demonstrated that the metal-free structures are rapidly destroyed under these reaction conditions. The central metal is thus essential for the stability of these macrocycles at demetallation conditions.

Shown in Fig. 5 is the variation in reactor outlet concentration as a function of contact time. Initially there is a rapid buildup of Ni-EPH_2 during which time there is a slight induction period in the rate of total metal removal. At all times the total metal in the oil (determined by atomic absorption) can be accounted for by summing the contributions of the Ni-EP and Ni-EPH_2 species (determined by visible spectra: Ni-EP, 557 nm; Ni-EPH_2, 616 nm).

Intrinsic kinetic parameters were evaluated using the reaction sequence in Fig. 2 assuming first-order reaction steps and constant hydrogen concentration in the oil. Rate constants used in the calculated solid line model results of Fig. 5 and their associated activation energies obtained from the Arrhenius plots in Fig. 6 are listed in Table 2. It is observed for Ni-Etio that hydrogenation of the porphyrin is the rate-limiting step in the overall demetallation scheme. The activation energies for the hydrogenation (k_1), dehydrogenation (k_2), and hydrogenolysis (k_3) steps are consistent with literature-reported values for similar reactions in hydrodenitrogenation (HDN) (*9*).

The large excess of hydrogen dissolved in the oil ensures that the hydrogen concentration remains constant and can therefore be lumped into the first-order rate coefficient. Variation of the hydrogen pressure during saturation of the oil permits the evaluation of the dependence of the rate coefficients on hydrogen pressure. Shown in Fig. 7 is such a determination for the three first-order rate coefficients k_1, k_2, and k_3 in the Ni-EP reaction scheme reported by Agrawal (*3*). Based on the slope of the line for k_1, a first-order dependence is observed. This is consistent with the observation that the first intermediate formed is the Ni-Etio chlorin, requiring the addition of one hydrogen molecule to the starting prophyrin. For a kinetically controlled dehydrogenation reaction, k_2 should be independent of hydrogen pressure and Fig. 7 confirms a zero-order dependence for this step. The final step, k_3, the metal-deposition reaction, exhibits second-order hydrogen dependence. This suggests that more than one hydrogen molecule is required for the final metal removal step and that a sequence of rapid reactions may be lumped into this hydrogenolysis step.

TABLE 2

Ni-Etioporphyrin

$$\text{Ni-EP} \underset{2}{\overset{1}{\rightleftharpoons}} \text{Ni-EPH}_2 \xrightarrow{3} \text{deposit}$$

Reaction conditions:
27 ppm Ni feed, 343°C, 6.99 MPa H_2 (1000 psig)

k_1 = 25.0 ml oil/g cat. hr	E_1 = 16.3 kcal/mole
k_2 = 100.0	E_2 = 20.5
k_3 = 80.0	E_3 = 28.7

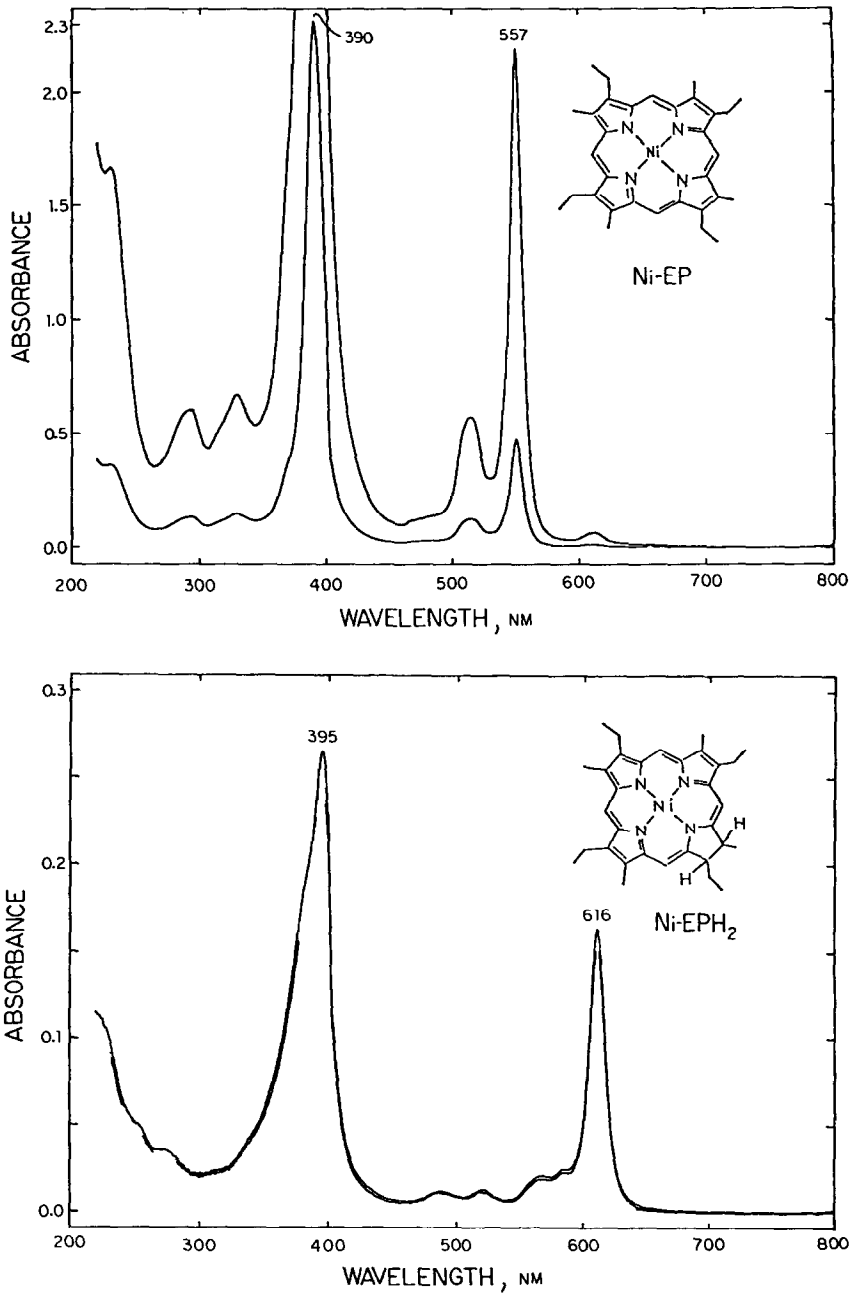

FIG. 4. Absorption spectra of Ni-etiporphyrin (top) and Ni-etiochlorin (bottom); background is hexane.

b. Ni-T3MPP

Investigation of the kinetics of Ni-T3MPP demetallation affords comparison with Ni-Etio of two porphyrins that have similar four pyrrole ring macrostructures and conjugation, 18 π electrons in delocalization pathway, but have structural differences around the periphery of the macrocycle (see Fig. 1). The higher solubility of Ni-T3MPP in Nujol (up to 120 ppm Ni) as compared to Ni-Etio (35 ppm Ni) also pro-

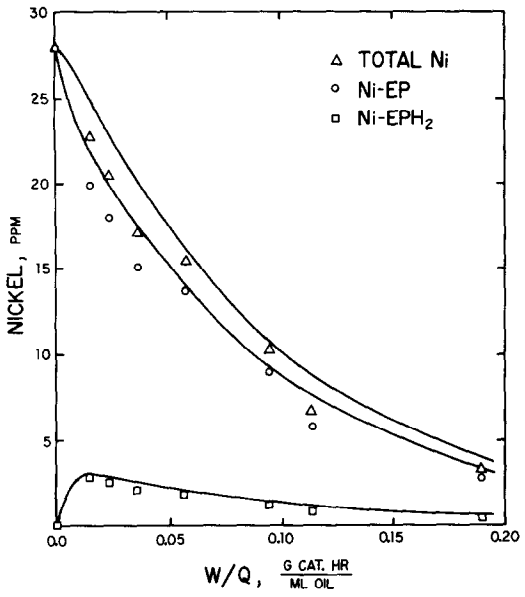

FIG. 5. Concentration versus contact time results for Ni-etioporphyrin at 27 ppm Ni feed, 343°C, and 6.99 MPa H_2 (1000 psig). Solid lines represent model calculations using parameter values in Table 2.

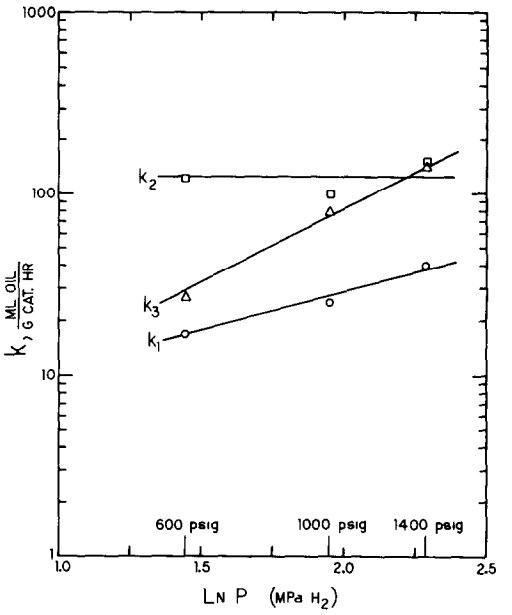

FIG. 7. Hydrogen-pressure dependence for the first-order rate parameters for Ni-etioporphyrin at 27 ppm Ni feed and 343°C.

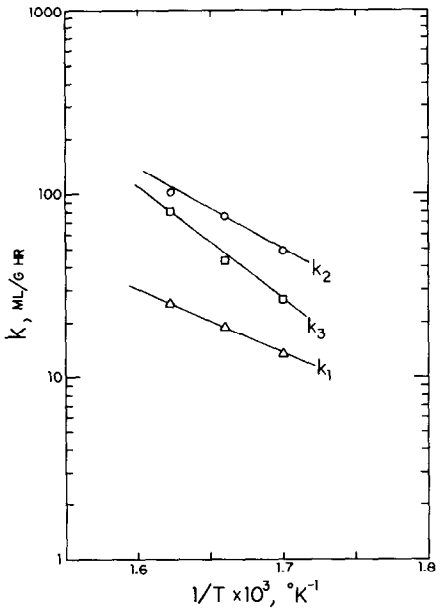

FIG. 6. Arrhenius plots for the first-order rate parameters for Ni-etioporphyrin at 6.99 MPa H_2 (1000 psig).

vides a more realistic metal loading in the "model" oil.

The uv–visible spectra of effluent oil shown in Fig. 8 reveals many absorption peaks indicating the presence of more stable intermediates as compared to Ni-Etio. The feed Ni-porphyrin is hydrogenated at one peripheral double bond resulting in Ni-chlorin formation (Ni-PH_2) followed by a second hydrogenation selectively at an adjacent pyrrole ring forming the Ni-isobacteriochlorin (Ni-PH_4). See Fig. 9 and Refs. (*14, 29*) for pure-component spectra and assignment of the peaks in Fig. 8. Central metals are observed to favor formation of adjacent tetrahydroporphyrins, the isobacteriochlorins, as opposed to opposite tetrahydroporphyrins known as the bacteriochlorins (*10*).

Typical concentration versus contact time data for Ni-T3MPP demetallation at a feed concentration of 63 ppm Ni are shown in Fig. 10. The figure shows the rapid disappearance of feed porphyrin (Ni-P) concurrently with the rapid production of Ni-PH_2

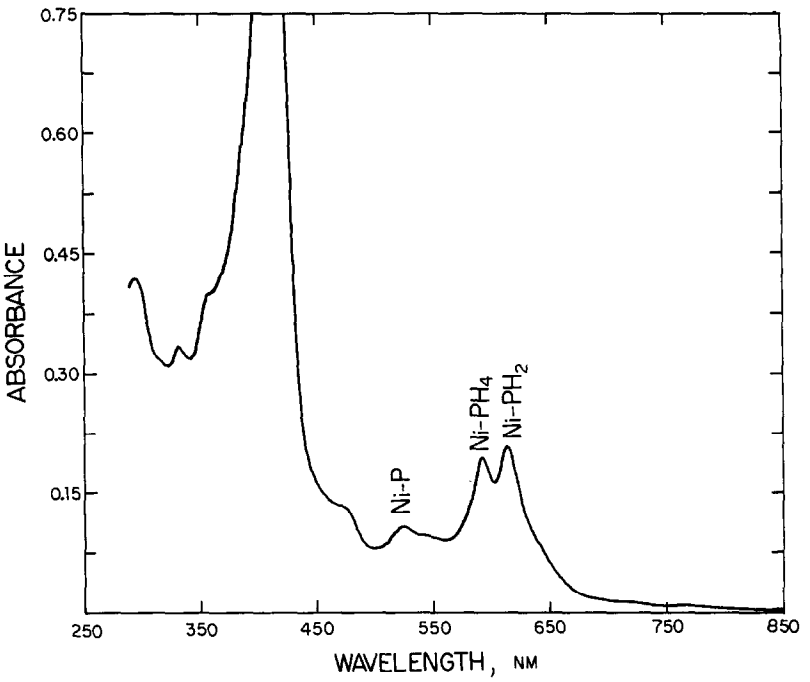

FIG. 8. Absorption spectra of effluent oil sample during HDM of Ni-tetra(3-methylphenyl)porphyrin at 345°C and 6.99 MPa H_2 (1000 psig); background is xylene.

and Ni-PH_4 followed by their more gradual removal. Beyond a critical W/Q value, 0.04 g cat. hr/ml in Fig. 10, the Ni-P/Ni-PH_2 and Ni-PH_2/Ni-PH_4 ratios remain constant, indicating that a dynamic equilibrium has been established between the porphyrinic species. The most striking feature of this figure is that the sum of the porphyrinic species in the effluent oil (concentration determined by visible absorption peaks: Ni-P, 526 nm; Ni-PH_2, 616 nm; Ni-PH_4, 593 nm) does not account for the total metal concentration in the oil determined by atomic absorption spectrophotometry. The discrepancy is represented by the symbol ϕ. At 95% Ni-T3MPP conversion only 20% of the total metal in solution can be accounted for by porphyrinic species (Ni-P, Ni-PH_2, Ni-PH_4). Examination of effluent oil uv–visible spectra at the high porphyrin conversions presented in Fig. 11 reveals no dominating absorption peaks at 400 nm indicating that the Ni unaccounted for is not present in a porphyrinic form, since macrocyclic conjugation has a characteristic strong absorption band at this wavelength (*11*).

HPLC analysis of effluent oil samples at high porphyrin conversions with especially poor metal balances revealed a component in addition to the porphyrinic (NiP, $NiPH_2$, $NiPH_4$) species. The uv–visible spectra of this compound taken during LC analysis is shown in Fig. 11 along with the composite spectra of effluent oil from which the injected sample was taken. The absorption peaks of this particular species correspond exactly to the maxima in the effluent oil scan, indicating that this is the dominant species in the oil. Atomic absorption analysis has confirmed that this compound can essentially account for the remaining nickel in the metal balance, hereinafter termed Ni-*X*.

The mass spectrum of this nickel intermediate reveals a parent molecular ion (M + 1) at m/e = 633. The presence of nickel is confirmed by the paired peaks at 633 (Ni^{58}) and 635 (Ni^{60}) corresponding to the nickel

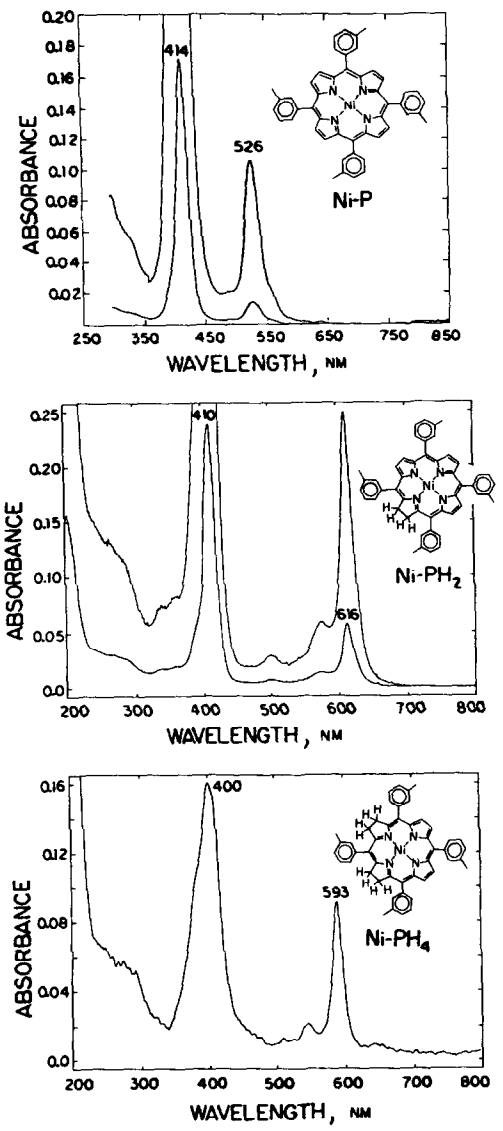

FIG. 9. Absorption spectra of Ni-tetra(3-methylphenyl)porphyrin (top), Ni-T3MP chlorin (middle), and Ni-T3MP isobacteriochlorin (bottom); background is hexane.

isotopes in the ratio of 2.5/1. This molecular weight is similar to that obtained by removing a toluene group from the starting porphyrin but several factors rule out this possible interpretation for Ni-*X*. The actual molecular weight of such a species corresponds to m/e = 636 (= 726 − 90). Hence the removal of four additional hydrogens from an already unsaturated species would be required. This is an unlikely occurrence considering both the nature of the molecule and the strong reducing environment of the reactions. The loss of a toluene group would also not be expected to reduce the macrocyclic conjugation of the porphyrin ring.

Further information is obtained by comparing the infrared absorbance bands in the region 1800 to 900 cm^{-1} for the nickel intermediate and the starting porphyrin, Ni-T3MPP, shown in Fig. 12. The increased number of bands in this region for Ni-*X* is an indication of lower symmetry which would result from hydrogenation or structural alteration of the starting porphyrin. The appearance of the 1470-cm^{-1} band and 1550-cm^{-1} shoulder have been assigned to —C=N— and —C=C— stretching vibrations which are forbidden or very weak in the highly symmetric D_{4h} porphyrin system (*12*). Similarly, strong bands in the Ni-T3MPP spectra at 1010 and 1352 cm^{-1} as-

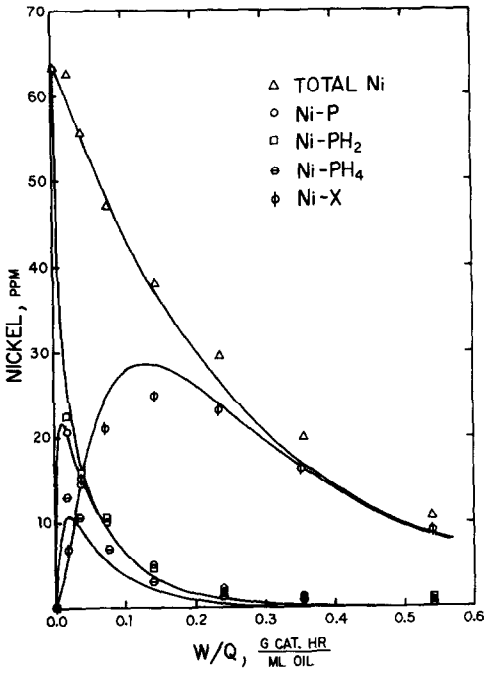

FIG. 10. Concentration versus contact time results for Ni-T3MPP at 63 ppm Ni feed, 345°C, and 6.99 MPa H_2 (1000 psig). Solid lines represent model calculations using parameter values in Table 3.

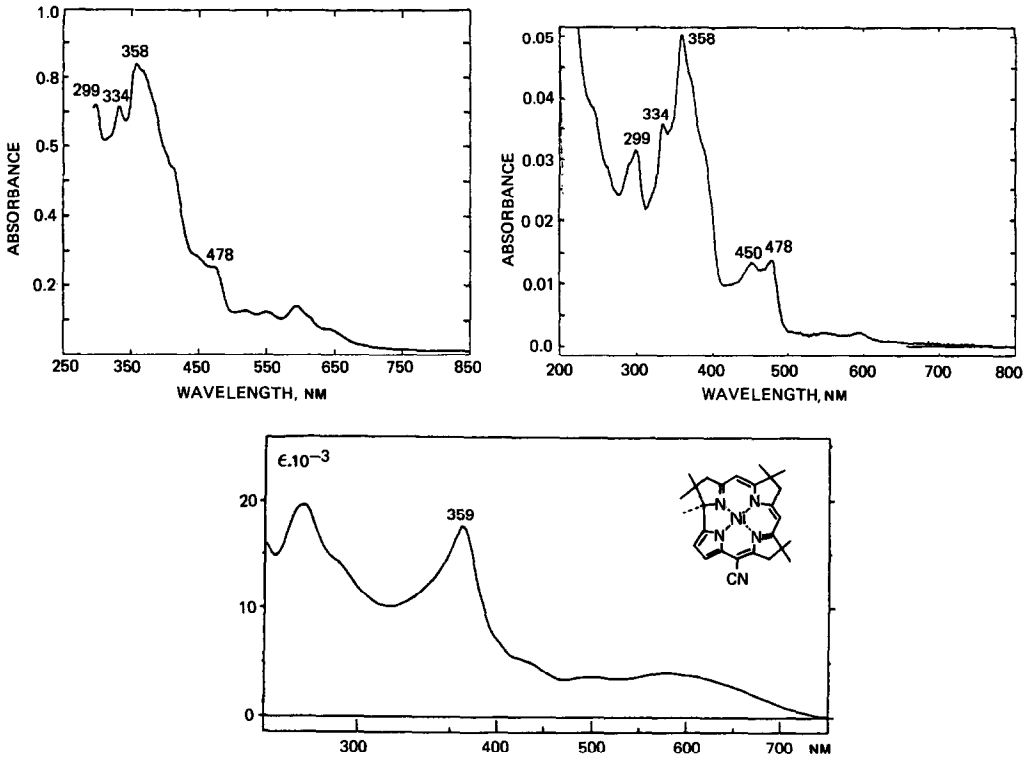

FIG. 11. Absorption spectra of effluent oil sample at high Ni-T3MPP conversion (top left), Ni-*X* species isolated from this oil sample during HPLC analysis (top right), and Ni-corrin-type species from Rasetti (*17*) (bottom); background is hexane.

signed to porphyrin macrocyclic ring vibration (*13*) and —C—N= vibrations of high double-bond character (*12*), respectively, are absent in the Ni-*X* spectra. Bands at ~1010 cm^{-1} have been reported for dihydrogenated and hexahydrogenated nickel porphyrins indicating that reduction alone does not eliminate this characteristic ring vibration (*14*). Furthermore, the presence of phenyl groups on the Ni-*X* species is indicated by the band at 1603 cm^{-1} which is likewise strong in Ni-T3MPP (*12*).

The analytical results suggest that the Ni-*X* intermediate results from a concerted reaction involving contraction of the ring at a bridge position adjacent to one of the hydrogenated pyrrole rings of Ni-PH_4 by elimination of the methine carbon as a xylyl group. The central nickel metal is known to exert a strong templating affect in such cyclizations by ensuring a favorable positioning between the adjacent α-pyrrolic carbon atoms (*15*). Similar reactions are common in the synthesis of analogous contracted ring structures referred to as metallo-corrins. A sequence to interpret this ring contraction route is depicted in Fig. 13. The initial step involves hydrogenation of a *meso* bridge adjacent to a hydrogenated pyrrole ring in Ni-PH_4 followed by opening of the ring by a concerted electrocyclic reaction (*15*). As will be discussed later, the *meso* positions on hydrogenated porphyrin rings are highly reactive. The key step in the sequence which follows involves an acid-catalyzed ring contraction step (*15, 16*) with subsequent elimination of the former bridge position carbon atom as a xylyl group.

For the case at hand, the molecular weight of this newly generated species is 628 indicating that the actual Ni-*X* interme-

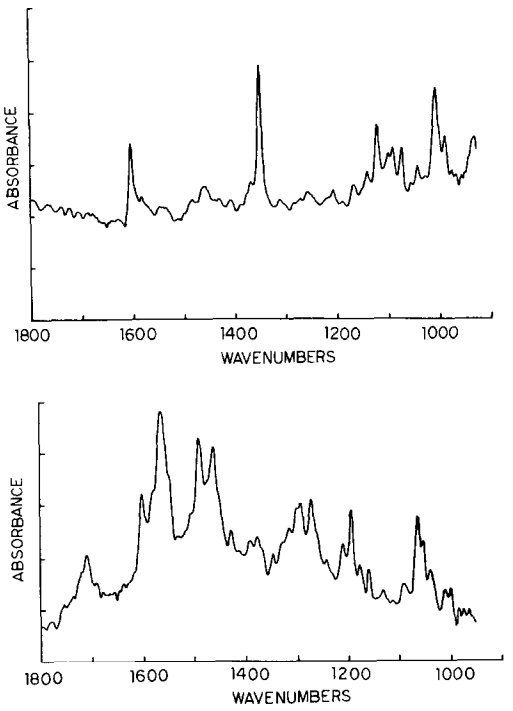

FIG. 12. Infrared spectra of Ni-T3MPP (top) and Ni-*X* (bottom). Samples referenced to tetrachloroethylene.

diate has undergone further hydrogenation after elimination of the xylyl group. The maxima in visible spectra of the Ni-*X* intermediate presented in Fig. 11 show resemblance to that of a nickel-corrin hydrogenated at additional pyrrole positions (*17*). These may likewise be the hydrogenated sites in the Ni-*X* molecule. The lack of any evidence for a Ni-PH_6 species in the oil [visible absorption peak at 670 nm (*18*)] is an indication that this hydrogenation occurs after ring contraction.

Several features of the proposed Ni-*X* structure shown in the reaction scheme of Fig. 13 are consistent with the observed analytical and experimental results. Foremost is the agreement between lack of macrocyclic conjugation detected in the visible spectra of this species and the corresponding interrupted porphyrin ring structure with extensive hydrogenation. Additionally, the ir spectrum is characterized by the absence of porphyrin ring vibrational modes and a decrease in molecular symmetry. Absorbance bands reported for con-

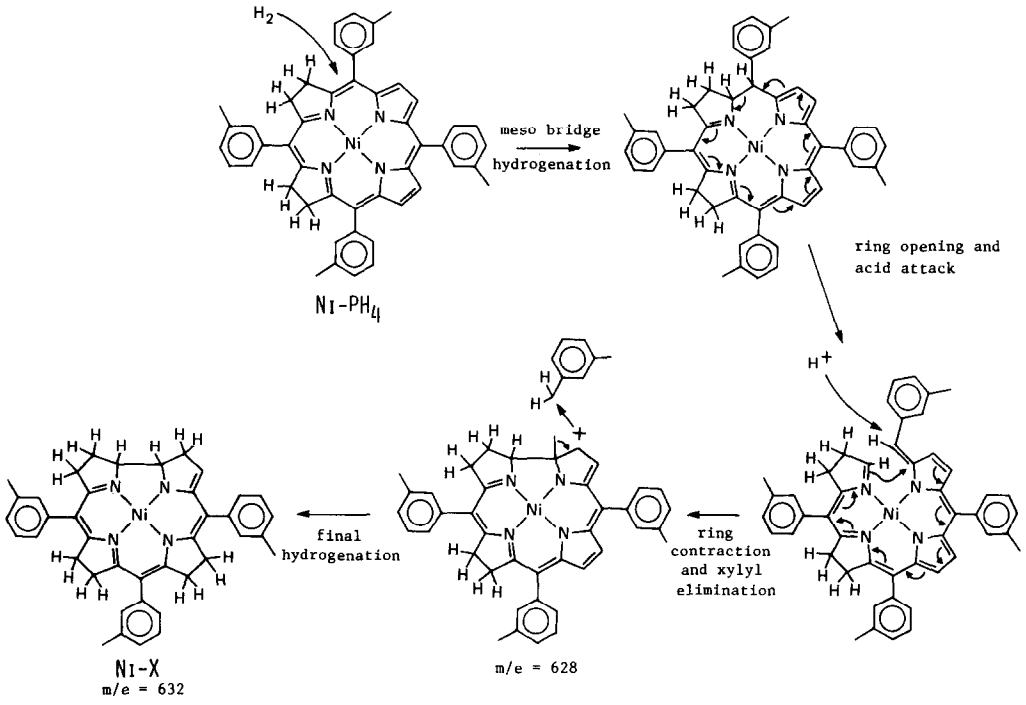

FIG. 13. Proposed sequence for ring contraction and Ni-*X* formation.

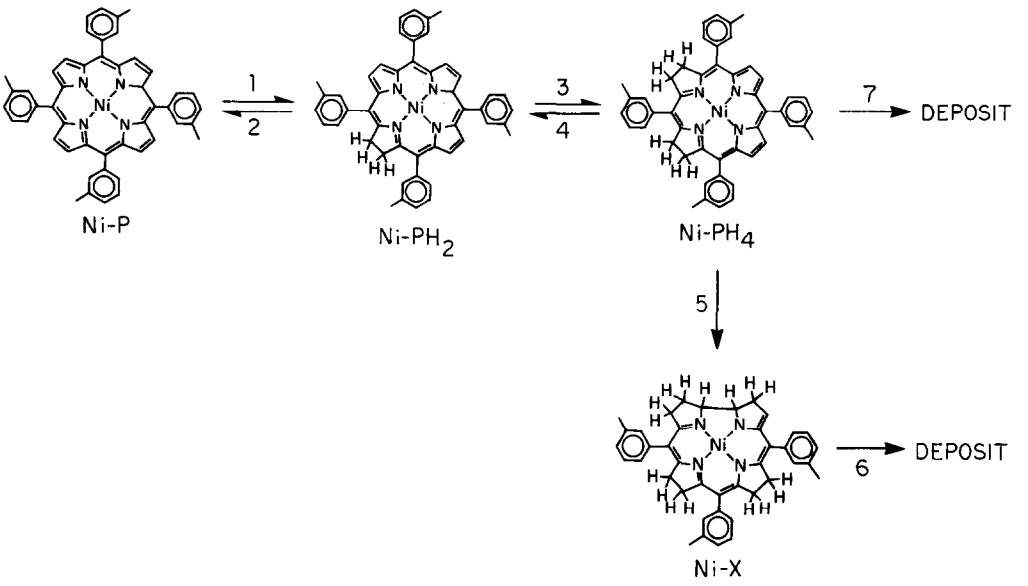

FIG. 14. Reaction sequence for Ni-tetra(3-methylphenyl)porphyrin.

tracted ring systems at 1566 cm^{-1} (*19*) and 1500 cm^{-1} (*20*) also appear identically at 1566 cm^{-1} and as a shoulder at 1500 cm^{-1} in the Ni-*X* sample. The nickel, verified by both atomic absorption and mass spectra, is retained in a square planar configuration with the four nitrogen atoms analogous to its coordination in the starting porphyrin. This indicates that no dramatic structural rearrangements were required during the formation of this species. Finally, the relatively slow reactivity of this nickel intermediate to demetallation is consistent with the reported observation that ring contraction stabilizes the metal–nitrogen bonds when the central metal is small enough to allow such a contraction (*21*). The coordination cavity of the corrin-type ligand system is closer to the spatical coordination optimum of the Ni^{2+} metal ion than the cavity of the hydrogenated porphyrin ligand (*22*).

Analysis of the total metal concentration as a function of *W*/*Q* for Ni-T3MPP demetallation in Fig. 10 revealed a discrepancy when attempting to interpret the behavior in terms of a single deposition step through Ni-*X*. In this figure the steepest slope on the total nickel curve (corresponding to the fastest rate of metal removal) occurs at short contact times when the oil–metal balance nearly closes with Ni-P, Ni-PH_2, and Ni-PH_4 and the Ni-*X* concentration is low. At longer contact times when the concentration of Ni-*X* is the largest and comprises essentially all metal in the oil, the rate of total metal removal is slower. Hence a route for metal deposition other than from the Ni-*X* species alone is required. A semilogarithmic plot of the total nickel concentration data contained in Fig. 10 does in fact reveal two straight-line regimes indicative of two first-order removal rates.

The kinetics of Ni-T3MPP demetallation have been modeled as a sequence of first-order reactions in the network shown in Fig. 14. Feed porphyrin is successively and reversibly hydrogenated twice to form the tetrahydro species. This Ni-PH_4 can then react via two paths, one leading to direct deposition of nickel on the catalyst surface and the other leading to formation of the stable Ni-*X* intermediate. The relative ratio of these two reactions may be dependent on the proximity of the molecule to both a hydrogenation and an acid site which are speculated to be necessary for ring contrac-

tion. The direct deposition step k_7 is analogous to the direct deposition of metal from Ni-EPH_2 in the Ni-Etio sequence. The formation of the Ni-X intermediate via reaction k_5 results in production of a pool of relatively unreactive nickel in the oil and determines the rate of the total metal removal at the higher contact times as evidenced by the parallel disappearance of Ni-X and total metal.

The coupled set of rate expressions for this model are solved by use of the Wei–Prater technique (*23*). Kinetic parameters used in the solid line model calculation of Fig. 10 are listed in Table 3. In contrast to Ni-Etio, hydrogenation of Ni-T3MPP is rapid and the hydrogenolysis steps k_6 and k_7 are rate determining in the demetallation sequence. Activation energies for the rate parameters at 63 ppm Ni feed are obtained

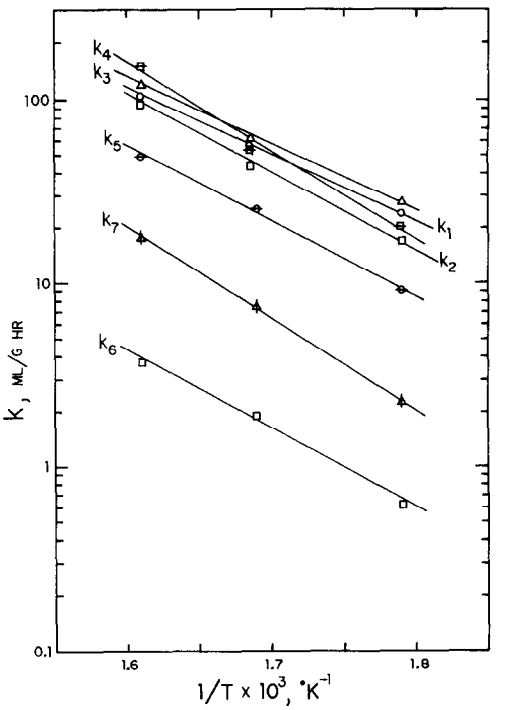

FIG. 15. Arrhenius plots for the first-order rate parameters for Ni-T3MPP at 63 ppm Ni feed and 6.99 MPa H_2 (1000 psig).

TABLE 3

Ni-Tetra(3-methylphenyl)porphyrin

$$\text{Ni-P} \underset{2}{\overset{1}{\rightleftharpoons}} \text{Ni-PH}_2 \underset{4}{\overset{3}{\rightleftharpoons}} \text{Ni-PH}_4 \xrightarrow{7} \text{deposit}$$

$$\text{Ni-PH}_4 \xrightarrow{5} \text{Ni-}X \xrightarrow[6]{} \text{deposit}$$

Reaction conditions: 345°C, 6.99 MPa H_2 (1000 psig)

Rate coefficient (ml oil/g cat. hr)	Feed concentration (ppm Ni)			
	16	26	63	90
k_1	86.0	85.0	105.0	94.0
k_2	100.0	90.0	94.0	84.0
k_3	120.0	130.0	120.0	130.0
k_4	145.0	150.0	150.0	155.0
k_5	55.0	66.0	49.0	60.0
k_6	4.20	4.60	3.80	4.25
k_7	24.0	25.0	18.0	19.5
Activation energy (kcal/mole)				
E_1		17.8	16.4	
E_2		21.8	20.0	
E_3		18.9	17.3	
E_4		23.1	21.2	
E_5		21.2	19.0	
E_6		20.0	20.0	
E_7		24.0	23.3	

from the Arrhenius plots of Fig. 15. Values likewise determined at 26 ppm Ni feed (Arrhenius plots not shown) were similar to the activation energies for the seven steps at the higher concentration.

Kinetic rate parameters determined for Ni-T3MPP were independent of feed concentration from 16 to 90 ppm Ni suggesting weak Ni-porphyrin absorption interactions with the catalyst (*25*). The slight kinetic parameter variations observed in Table 3 are attributed to different levels of activity and metals deposits. At the end of each run the Ni loading varied from 0.67 wt% for the 16 ppm Ni run to 3.7 wt% Ni for the 90 ppm Ni experiment.

The hydrogen-pressure dependence of the rate coefficients presented in Fig. 16 was similar to that for Ni-etioporphyrin. Over the pressure range 4.58–10.09 MPa H_2 (650–1450 psig) the hydrogenation steps k_1 and k_3 exhibited first-order hydrogen dependence whereas the dehydrogenation

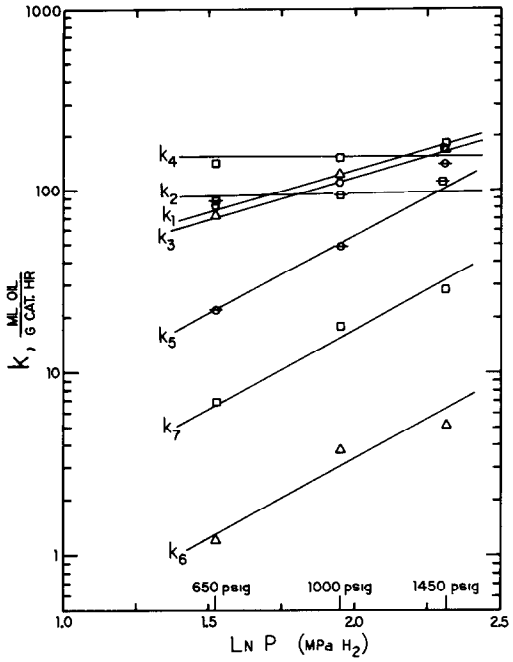

FIG. 16. Hydrogen-pressure dependence for the first-order rate parameters for Ni-tetra(3-methylphenyl)porphyrin at 63 ppm Ni feed and 345°C.

steps k_2 and k_4 were independent of hydrogen pressure. Step k_5 exhibited second-order hydrogen dependence. The proposed structure for the Ni-*X* intermediate is consistent with the requirement for the addition of more than one hydrogen molecule in its formation from Ni-PH_4. Likewise, the final metal-deposition steps k_6 and k_7 exhibited second-order dependence.

c. Ni-TPP

The behavior of Ni-TPP under HDM conditions is similar to that of Ni-T3MPP. The *meta*-substituted methyl groups on the phenyl rings are observed to have little effect on the porphyrin reactivity.

Total metal removal kinetics for Ni-TPP on $CoMo/Al_2O_3$ were first reported by Hung (*2*) in his model compound hydrodemetallation work. At that stage, the importance of intermediates in the overall demetallation scheme were not fully appreciated. Ultraviolet–visible spectra of effluent oil samples, however, revealed the presence of absorption peaks at 616 and 593 nm characteristic of the Ni-PH_2 and Ni-PH_4 species. Reexamination of Hung's batch data indicates that like Ni-T3MPP, the porphyrinic fraction fails to account for all metal in effluent oil. At 90% Ni-TPP conversion under reaction conditions of 344°C and 6.99 MPa H_2 (1000 psig), only 20% of the Ni in the oil can be accounted for by the Ni-P, Ni-PH_2, and Ni-PH_4 components.

5. KINETIC DISCUSSIONS

The model compound results have demonstrated the sequential nature of hydrodemetallation on the oxide form of $CoMo/Al_2O_3$. The initial ring hydrogenation of the pyrrole group appears to be the pathway resulting in the least disruption of the porphyrin molecule. The porphyrin aromaticity is not significantly interrupted since only 18 of the original 22 π electrons in the porphyrin are included in any one delocalization pathway (*11*). The different degrees of hydrogenation observed between Ni-Etio and Ni-T3MPP (also Ni-TPP) can be rationalized in terms of porphyrin basicity and steric factors. The electron-donating effect of the methyl and ethyl groups in Ni-Etio renders the β-pyrrolic positions more basic and hence less susceptible to electron addition occurring upon reduction than Ni-T3MPP where only hydrogen atoms exist at these positions. The larger β-pyrrolic substituents in Ni-Etio would also appear to hinder access to the catalytic hydrogenation sites. Reduction potentials, directly related to basicity, are a commonly used parameter in correlating porphyrin reactivity (*26*). Reduction potential values determined by Hambright (*27*) are lower for Ni-T3MPP as compared to Ni-Etio, implying that Ni-T3MPP should be more readily reduced as has been observed.

A more significant result than the slight disruption of aromaticity resulting from porphyrin hydrogenation is the enhancement in reactivity of the methine bridges adjacent to the newly formed pyrroline ring toward electrophilic attack (*28–30*). In the

porphyrin macrocycle, the four pyrrolic rings are maintained as aromatic subunits by borrowing electron density from neighboring methine bridges. The reduced pyrrole ring in the chlorin is no longer such a subunit and thus the electron density at the neighboring methine positions is increased.

Kwart *et al.* (*31*) have recently proposed a mechanism for HDS on sulfided CoMo/Al_2O_3 catalysts. A similar interpretation is useful to explain the HDM behavior observed in this study on oxide CoMo/Al_2O_3. The hydrogenated porphyrins presumably interact at the highly reactive methine bridges adjacent to the pyrroline ring with Mo anion vacancies. Interaction of π electrons with the metal would lead to transformation of the C–C π bond to yield a σ bond which at the same time would activate the methine bridge for hydrogenation. Once the aromaticity of the bridge has been destroyed by hydrogenation, stabilization of the molecule by macrocyclic conjugation is lost. The resulting strain in the now sp^3 α-pyrrolic carbon atom may favor cleavage of the ring and formation of an open ring metallo-tetrapyrrole structure (*30*). One possible route for this reaction would be a concerted 18π-electron electrocylic reaction (*15*). The presence of an acidic catalyst may likewise facilitate this cleavage via a carbonium ion cracking mechanism. Similar open-chain tetrapyrrolic structures (M-biliverdinates) have been found to be unstable under catalytic hydrogenating conditions (*32*).

With Ni-Etio, the lack of stable intermediates (other than the chlorin) detected indicates that this sequence proceeds rapidly when the methine bridges are open and exposed to attack.

In contrast to Ni-Etio, the reaction of Ni-T3MPP may be interpreted as resulting from the influence exerted by the tolyl groups at the methine bridges. Their presence sterically hinders interaction of the methine bridge sites with the catalyst resulting in inhibition of the hydrogenation of the double bond and the subsequent cleavage step. A second influence is the ability of the tolyl group to stabilize the methine carbon as a leaving group during formation of the nickel-corrin-type intermediate, the Ni-*X*. The success of the central nickel in exerting a templating effect to contract the ring is apparent by the k_5/k_7 ratios consistently greater than one. Accompanying this bridging of the two α-carbon atoms in the adjacent pyrrole rings is the simultaneous elimination of the former methine carbon as a xylyl group. This reaction occurring to relieve the steric crowding at the contracted bridge bond.

The cleavage of the carbon–carbon bond in this sequence, beta to the tolyl ring, is a reaction commonly encountered in carbonium ion and free-radical reactions. This same ring contraction/carbon elimination reaction, were it to occur with N-etioporphyrin, would involve loss of a methyl group. Formation of a methyl carbonium ion, for example, is energetically 50 kcal/mole higher than the corresponding xylyl carbonium ion and hence highly unfavorable (*33*). This may explain in part the absence of the analogous nonporphyrinic nickel intermediate in the demetallation of Ni-etioporphyrin on CoMo/Al_2O_3.

6. METAL-DEPOSITION RESULTS

Metal-deposition profiles measured in catalysts from commercial hydroprocessing units reveal that HDM reactions are diffusion limited. Vanadium tends to be deposited in sharp, U-shape profiles (*34, 35*) whereas nickel has been observed in both U-shape (*35*) and uniform (*34*) profiles. Agrawal (*3*) and Tamm *et al.* (*4*) have shown that metal-deposition profiles depend on the axial location of the catalyst within the reactor. Nickel and vanadium both exhibited profiles with internal maxima, termed M-shape, at the reactor entrance. These maxima were found to shift to the pellets' edge at the reactor outlet, generating the classical U-shape profile.

Nickel-deposition profiles obtained with Ni-Etio and with Ni-T3MPP as a function

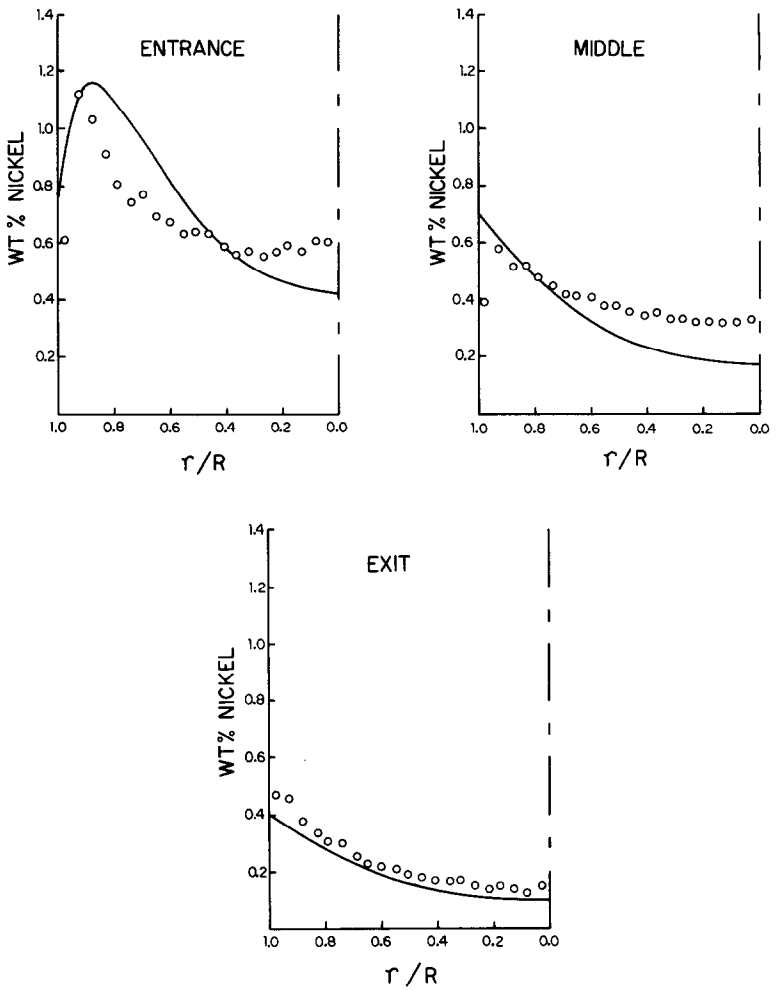

FIG. 17. Nickel-deposition profiles in 1/16-in.-diameter catalyst pellets at various reactor axial positions from Ni-etioporphyrin demetallation at 345°C and 6.99 MPa H_2 (1000 psig). Solid lines represent model calculations using parameter values in Table 4.

of axial position are presented in Figs. 17 and 18. Experimental points are represented by the open circles. At the reactor entrance, no metal-depositing species are present in the oil. The nickel porphyrins must first react to form the metal-depositing intermediates before metal accumulates on the pellets. As feed material diffuses into the first catalyst particles and reacts, the concentration of intermediates rises and the M-shape profiles appear. The position of the internal maxima within the first pellets is determined by the reaction network, the temperature, and the hydrogen pressure.

The internal maximum at the reactor entrance for Ni-T3MPP, shown in Fig. 18, is well pronounced compared to that for Ni-Etio, shown in Fig. 17. The maximum occurs at $r/R = 0.75$ whereas for Ni-Etio it is at 0.90. This is easily explained in terms of the longer HDM sequence and the slow metal removal steps previously discussed for Ni-T3MPP. The Ni-T3MPP metal profiles are also relatively uniform in the inner half of the pellets. This is a direct result of the two metal-deposition routes characteristic of Ni-T3MPP. The fast reaction (k_7) operates under strong diffusional limita-

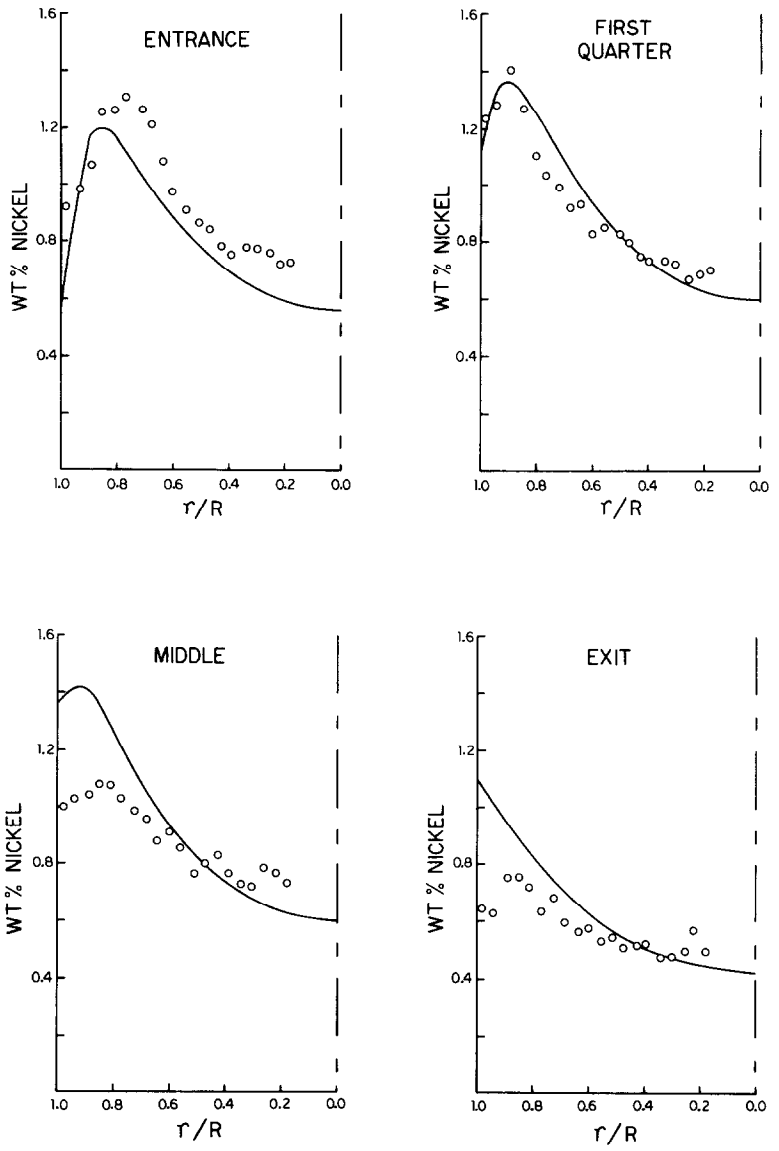

FIG. 18. Nickel-deposition profiles in 1/16-in.-diameter catalyst pellets at various reactor axial positions from Ni-T3MPP demetallation at 345°C and 6.99 MPa H_2 (1000 psig). Solid lines represent model calculations using parameter values in Table 5.

tions giving rise to the high metal loadings at the edge whereas the slow deposition step (k_6), less influenced by diffusional effects, dominates in the center.

The pattern of metal deposition is useful as a fingerprint of the HDM kinetic scheme and reflects the radial position of metal-bearing intermediates just prior to deposition. The profiles have been modeled using the theory of coupled multicomponent first-order reaction and diffusion given by Wei (*36*). The approach used for the Ni-T3MPP kinetic scheme will be outlined; that for the Ni-Etio scheme has been given elsewhere (*3*). The steady-state equations for diffusion with the hydrodemetallation scheme

TABLE 4

Parameters for Ni-Etioporphyrin Metal Profile Modeling (Fig. 17)

k_1 = 25.0 ml oil/g cat. hr	t = 75 hr
k_2 = 100.0	ρ = 0.88 g/ml
k_3 = 80.0	ρ_c = 1.49 g/ml
$D_1 = 2.5 \times 10^{-6}$ cm²/sec	Q = 15.0 ml/hr
$D_2 = 4.8 \times 10^{-6}$	W = 5.0 g
	R = 0.076 cm
	C_0 = 32.0 ppm Ni

Effluent oil concentration

	Experimental	Calculated
Ni-EP	4.8 ppm Ni	4.7
Ni-EPH$_2$	0.70	0.63
	5.5	5.33

can be written as

$$\frac{1}{\rho_c}\begin{bmatrix} D_1 & 0 & 0 & 0 \\ 0 & D_2 & 0 & 0 \\ 0 & 0 & D_3 & 0 \\ 0 & 0 & 0 & D_4 \end{bmatrix} \nabla^2 \begin{bmatrix} C_1 \\ C_2 \\ C_3 \\ C_4 \end{bmatrix} = \begin{bmatrix} k_1 & -k_2 & 0 & 0 \\ -k_1 & (k_2 + k_3) & -k_4 & 0 \\ 0 & -k_3 & (k_4 + k_5 + k_7) & 0 \\ 0 & 0 & -k_5 & k_6 \end{bmatrix} \begin{bmatrix} C_1 \\ C_2 \\ C_3 \\ C_4 \end{bmatrix}, \quad (1)$$

where C_1, C_2, C_3, and C_4 are the concentrations in ppm Ni of Ni-P, Ni-PH$_2$, Ni-PH$_4$, and Ni-X, respectively, inside the catalyst pellet and D_1, D_2, D_3, and D_4 the respective effective diffusivities in cm²/sec. These diffusion coefficients are assumed to be constant on the basis that the low level of deposited nickel is not sufficient to restrict diffusion in the catalyst pores. The rate coefficients, k (in units of ml oil/g cat. hr), are from the kinetic scheme previously discussed. The catalyst density, ρ_c, is necessary to balance the units. The boundary conditions accompanying Eq. (1) are

$$r = 0 \qquad \nabla \begin{bmatrix} C_1 \\ C_2 \\ C_3 \\ C_4 \end{bmatrix} = 0$$

$$\text{and } r = R, \qquad \begin{bmatrix} C_1 \\ C_2 \\ C_3 \\ C_4 \end{bmatrix} = \begin{bmatrix} C_{1s} \\ C_{2s} \\ C_{3s} \\ C_{4s} \end{bmatrix}, \quad (2)$$

where the subscript s refers to the concentration in the oil at the outer surface of the catalyst.

The solution to the above set of equations and appropriate boundary conditions for cylindrical geometry is given by

$$\begin{bmatrix} C_1 \\ C_2 \\ C_3 \\ C_4 \end{bmatrix} = \bar{\mathbf{Y}} \begin{bmatrix} \frac{I_0(\phi_1 r/R)}{I_0(\phi_1)} & 0 & 0 & 0 \\ 0 & \frac{I_0(\phi_2 r/R)}{I_0(\phi_2)} & 0 & 0 \\ 0 & 0 & \frac{I_0(\phi_3 r/R)}{I_0(\phi_3)} & 0 \\ 0 & 0 & 0 & \frac{I_0(\phi_4 r/R)}{I_0(\phi_4)} \end{bmatrix} \bar{\mathbf{Y}}^{-1} \begin{bmatrix} C_{1s} \\ C_{2s} \\ C_{3s} \\ C_{4s} \end{bmatrix}, \quad (3)$$

where $\bar{\mathbf{Y}}$ and $\bar{\mathbf{Y}}^{-1}$ are the eigenvector matrix and the inverse matrix of the $\rho_c \bar{\mathbf{D}}^{-1}\bar{\mathbf{K}}$ matrix and I_0 the modified Bessel function of the first kind of zero order. Defining λ_1, λ_2, λ_3, and λ_4 as the eigenvalues of $\rho_c \bar{\mathbf{D}}^{-1}\bar{\mathbf{K}}$, then the Thiele modulus for each characteristic species is $\phi_i = \sqrt{\lambda_i} R$ for i = 1, 2, 3, 4, where R is the pellet radius.

Using the solution given by Eq. (3), the overall species reaction rates for each catalyst pellet can be obtained from the fluxes of reactants across the boundary. The rate

of reaction per unit mass of catalyst is then given by

$$\frac{2\pi RL\rho\bar{\mathbf{D}}\,\frac{d}{dr}\,\mathbf{C}\Big|_R}{\pi R^2 L\rho_c} = \frac{2\rho\bar{\mathbf{D}}}{R^2\rho_c}\,\bar{\mathbf{Y}}\left\{\bar{\phi}\,\frac{I_1(\bar{\phi})}{I_0(\bar{\phi})}\right\}\bar{\mathbf{Y}}^{-1}\mathbf{C}_s, \quad (4)$$

where L is the pellet length and ρ the oil density.

This flux expression may be reduced to

$$\rho\bar{\mathbf{K}}^{+}\mathbf{C}_s,$$

where $\bar{\mathbf{K}}^{+}$ is the diffusion-disguised overall rate coefficient matrix based on the bulk oil concentrations given by

$$\bar{\mathbf{K}}^{+} = \frac{2\bar{\mathbf{D}}}{R^2\rho_c}\,\bar{\mathbf{Y}}\left\{\bar{\phi}\,\frac{I_1(\bar{\phi})}{I_0(\bar{\phi})}\right\}\bar{\mathbf{Y}}^{-1}. \quad (5)$$

The problem then is simply one of using this local rate expression in a differential material balance in the reactor. For a plug flow reactor assuming uniform catalyst distribution and no interphase transport resistances, the set of mass balances is given by

$$Q\,\frac{d\mathbf{C}_s}{dW} = -\bar{\mathbf{K}}^{+}\mathbf{C}_s, \quad (6)$$

where Q is the volumetric oil flow rate and dW the differential weight of catalyst along the reactor length. The initial condition for Eq. (6) is the feed composition to the reactor:

$$\text{at } W = 0 \qquad \begin{bmatrix} C_{1s} \\ C_{2s} \\ C_{3s} \\ C_{4s} \end{bmatrix} = \begin{bmatrix} C_0 \\ 0 \\ 0 \\ 0 \end{bmatrix}. \quad (7)$$

Integrating Eq. (6) over the total weight of catalyst, W, yields

$$\begin{bmatrix} C_{1s} \\ C_{2s} \\ C_{3s} \\ C_{4s} \end{bmatrix} = \bar{\mathbf{X}}^{+}\begin{bmatrix} \exp(-\lambda_1^{+}\,W/Q) & 0 & 0 & 0 \\ 0 & \exp(-\lambda_2^{+}\,W/Q) & 0 & 0 \\ 0 & 0 & \exp(-\lambda_3^{+}\,W/Q) & 0 \\ 0 & 0 & 0 & \exp(-\lambda_4^{+}\,W/Q) \end{bmatrix}\bar{\mathbf{X}}^{+-1}\begin{bmatrix} C_0 \\ 0 \\ 0 \\ 0 \end{bmatrix}, \quad (8)$$

where $\bar{\mathbf{X}}^{+}$ and $\bar{\mathbf{X}}^{+-1}$ are the eigenvector matrix and the inverse matrix of the diffusion-disguised rate constant matrix $\bar{\mathbf{K}}^{+}$, and λ_1^{+}, λ_2^{+}, λ_3^{+}, and λ_4^{+} are its characteristic eigenvalues. With Eq. (8) it is possible to calculate the concentration profiles in the bulk oil through the reactor as a function of catalyst weight (or equivalently, reactor length).

Concentration distributions within individual catalyst pellets at specific axial positions are determined from Eq. (3) using the bulk oil concentration given by Eq. (8). The final step, the calculation of the amount of deposited metal as a function of pellet radius at any position along the reactor, is accomplished using

$$M = [k_6C_4 + k_7C_3]\rho t \times 10^{-4}, \quad (9)$$

where M is the weight percentage deposited nickel and t the reactor time on stream in hours. The factor of 10^{-4} is necessary when the units of concentration are in parts per million. The two routes to metal deposition

with Ni-T3MPP are clearly identified in Eq. (9).

The kinetic rate parameters used in solving Eqs. (3) and (8) have been independently determined in the intrinsic studies leaving the four diffusion coefficients as the only unknowns in these equations. Values for these parameters were then adjusted to obtain a best fit between the measured and predicted values of both the intrapellet metal profiles along the reactor length and the species concentration in the effluent oil. Listed in Table 5 are the parameter values used and the resulting effluent oil concentrations. Results from Ni-Etio modeling are presented in Table 4 and very good agreement was obtained between experimental and calculated concentrations.

7. METAL-DEPOSITION DISCUSSION

The predicted metal profiles are represented as the solid lines in Figs. 17 and 18. The model predicts the M-shape behavior for Ni-T3MPP with the maxima shifting to the edge of the pellet toward the end of the reactor. Similarly, the concentration of metal at the point of maximum loading within a pellet is predicted to increase, initially, with axial position before declining further down the length of the bed. This behavior has been observed experimentally. Both of these features are a direct consequence of the sequential metal-deposition pathway.

Quantitative agreement between predicted and experimental metal profiles is satisfactory, especially in the front half of the reactor when using unequal diffusivities for the nickel species. The best-fit values for the effective diffusivities are in the range $1\text{–}2 \times 10^{-6}$ cm^2/sec. An estimate for the values of the diffusion coefficients for the porphyrinic species can be obtained from the Stokes–Einstein equation. Assuming a molecular diameter for Ni-T3MPP of 15 Å, the bulk liquid-phase diffusivity in Nujol at 350°C is calculated to be 4.8×10^{-5} cm^2/sec. An effective diffusivity in the catalyst is obtained by correcting for configurational effects with the Spry and Sawyer (*37*) factor and by assuming a catalyst pore diameter of 80 Å, a void fraction of 0.5, and a tortuosity factor of 6. The resulting effective diffusivity is calculated to be 1.7×10^{-6} cm^2/sec.

The three porphyrinic species would be expected to have similar diffusivities based on size. The difference of a factor of 2 be-

TABLE 5

Parameters for Ni-Tetra(3-methylphenyl)porphyrin Metal Profile Modeling (Fig. 18)

k_1 = 105.4 ml oil/g cat. hr	$D_1 = 1.0 \times 10^{-6}$ cm^2/sec	t = 109 hr
k_2 = 94.0	$D_2 = 2.0 \times 10^{-6}$	ρ = 0.88 g/ml
k_3 = 120.0	$D_3 = 2.0 \times 10^{-6}$	ρ_c = 1.49 g/ml
k_4 = 150.0	$D_4 = 2.0 \times 10^{-6}$	Q = 15.0 ml/hr
k_5 = 49.0		W = 5.0 g
k_6 = 3.80		R = 0.076 cm
k_7 = 18.0		C_0 = 66 ppm Ni

Effluent oil concentration

	Experimental	Calculated
Ni-P	9.9 ppm Ni	6.3
Ni-PH_2	4.6	5.1
Ni-PH_4	2.6	3.0
Ni-*X*	17.5	18.7
	34.6	33.1

tween the values for Ni-P and Ni-PH_2, Ni-PH_4 while not large, was required to obtain a better fit to the metal profiles. It is conceivable that the strength of the interaction with the catalyst surface is different for the porphyrin and hydrogenated derivatives. This would alter the adsorption and surface diffusion processes for the species, both of which contribute to the observed effective diffusivity. The similarity of the Ni-*X* diffusion coefficient to those of the porphyrinic species suggests the size and surface interactions of this species, despite its being a contracted ring, are not all that different from the porphyrin.

The Ni-Etio metal profiles of Fig. 17 were modeled in a similar fashion. It was again determined that unequal diffusivities for Ni-EP and Ni-EPH_2 were needed to give an accurate representation of the metal profiles throughout the bed as well as the effluent oil concentration (see Table 4). The values for the diffusion coefficients were well within the expected range and of similar magitude, yet consistently larger than the Ni-T3MPP values, which was expected based on the smaller size of Ni-etioporphyrin.

The observed pattern of metal deposition serves as further proof of the sequential nature of hydrodemetallation reactions of nickel porphyrins on $CoMo/Al_2O_3$. An earlier interpretation suggested that the internal maximum at the entrance of the reactor was related to an increasing concentration of H_2S, speculated to be necessary for demetallation (*4*). The results presented here in the absence of sulfur demonstrate that the M-shaped metal-deposition pattern is solely a consequence of the reaction network of the metal species.

8. CONCLUSIONS

The reactivity of nickel porphyrins under hydrodemetallation conditions on an oxide $CoMo/Al_2O_3$ catalyst has been shown to involve a sequential mechanism. The porphyrins are initially hydrogenated, forming precursor species which subsequently react via hydrogenolysis steps to deposit the metal on the catalyst surface. Structural differences on the periphery of the metalloporphyrin molecules are shown to significantly influence the complexity of the reaction pathways and the relative rates of hydrogenation and hydrogenolysis. The substituent groups at the β-pyrrolic and methine bridge carbon atoms in the porphyrin appear to exert a dominant role, both steric and chemical, in determining these reactivity differences. Variations in the overall rate-limiting step for metal removal are possible from one porphyrin to the next but the global sequence of hydrogenation followed by hydrogenolysis is still preserved.

Radial nickel-deposition profiles in catalyst pellets obtained under diffusion-limited conditions are dependent on the axial location of the catalyst within the reactor. These profiles have been interpreted in terms of the sequential HDM reaction schemes developed for the porphyrins using diffusion coefficients for all the nickel species on the order of 10^{-6} cm^2/sec. Structural differences between nickel porphyrins which influence the intrinsic kinetics are likewise reflected in the metal-deposition patterns.

APPENDIX: NOMENCLATURE

C_0	initial nickel concentration, ppm
C_1, C_2, C_3, C_4	concentrations of Ni-P, Ni-PH_2, Ni-PH_4, and Ni-*X*, respectively, ppm
$\mathbf{C}$	concentration vector
D_1, D_2, D_3, D_4	effective diffusivity of Ni-P, Ni-PH_2, Ni-PH_4, and Ni-*X*, cm^2/sec
$\overline{\mathbf{D}}$	diffusion coefficient matrix of Eq. (1)
E	activation energy, kcal/mole

I_0	modified Bessel function of first kind of zero order
I_1	modified Bessel function of first kind of first-order
k	rate coefficient, ml oil/g cat. hr
$\bar{\mathbf{K}}$	rate coefficient matrix of Eq. (1)
$\bar{\mathbf{K}}^+$	diffusion-disguised rate coefficient matrix of Eq. (5)
L	length of catalyst pellet, cm
M	deposited metal, wt%
Q	oil flow rate, ml/hr
r	radial position, cm
R	pellet radius, cm
t	time on stream, hr
W	weight of catalyst, g
$\bar{\mathbf{X}}^+$, $\bar{\mathbf{X}}^{+-1}$	eigenvector matrix and inverse matrix of $\bar{\mathbf{K}}^+$
$\bar{\mathbf{Y}}$, $\bar{\mathbf{Y}}^{-1}$	eigenvector matrix and inverse matrix of $\rho_c\bar{\mathbf{D}}^{-1}\bar{\mathbf{K}}$
λ_i	ith eigenvalue of $\rho_c\bar{\mathbf{D}}^{-1}\bar{\mathbf{K}}$
λ_i^+	ith eigenvalue of $\bar{\mathbf{K}}^+$
ρ	oil density, g/ml
ρ_c	catalyst density, g/ml
ϕ_i	ith Thiele modulus $= \sqrt{\lambda_i}R$
$\bar{\phi} = \dfrac{I_1(\bar{\phi})}{I_0(\bar{\phi})}$	diagonal matrix of Eq. (5)
subscript s	catalyst pellet surface, $r = R$

ACKNOWLEDGMENTS

The authors are grateful to the following people for their assistance: David Green and Chi-Wen Hung of Chevron Research Company for their helpful discussions and, along with Jack T. Gilmore and Mark J. Meisner of Chevron Research Company, for providing the microprobe measurements in Figs. 17 and 18; Bill Dark of Waters Associates for providing technical assistance and the HPLC columns; James Bentsen for providing the ir spectra in Fig. 12; and Ian A. Webster for his helpful comments. The financial support of the National Science Foundation, Grant CPE 80-20852, and Chevron Research Company is also gratefully acknowledged.

REFERENCES

1. Speight, J. G., "The Desulfurization of Heavy Oils and Residua." Dekker, New York, 1981.
2. Hung, C. W., and Wei, J., *Ind. Eng. Chem. Process Des. Dev.* **19,** 250, 257 (1980).
3. Agrawal, R., "Kinetics and Diffusion in Hydrodemetallation of Nickel and Vanadium Porphyrins," Sc.D. thesis. M.I.T., August 1980; Agrawal, R., and Wei, J., *Ind. Eng. Chem. Process Des. Dev.* **23,** 505, 515 (1984).
4. Tamm, P. W., Harnsberger, H. F., and Bridge, A. G., *Ind. Eng. Chem. Process Des. Dev.* **20,** 262 (1981).
5. Rankel, L. A., *ACS Prepr. Div. Pet. Chem.* **26,** 689 (1981).
6. Kameyama, H., and Amano, A., *J. Jpn. Pet. Inst.* **25,** 118 (1982).
7. Baker, E. W., and Palmer, S. E., *in* "The Porphyrins" (D. Dolphin, Ed.), Vol. 1, Chap. 11. Academic Press, New York, 1978.
8. Vaughan, G. B., Tynan, E. C., and Yen, T. F., *Chem. Geol.* **6,** 203 (1970).
9. Satterfield, C. N., and Gultekin, S., *Ind. Eng. Chem. Process Des. Dev.* **20,** 62 (1981).
10. Scheer, H., *in* "The Porphyrins" (D. Dolphin, Ed.), Vol. 2, Chap. 1. Academic Press, New York, 1978.
11. Smith, K. M., *in* "Porphyrins and Metalloporphyrins" (K. M. Smith, Ed.), Chap. 1. Elsevier, Amsterdam, 1975.
12. Thomas, D. W., and Martell, A. E., *J. Amer. Chem. Soc.* **81,** 5111 (1959).
13. Kincaid, J., and Nakamoto, K., *J. Inorg. Nucl. Chem.* **37,** 85 (1975).
14. Angst, C., "New Hexahydroporphyrin Ligand Systems," Ph.D. thesis, Diss. ETH No. 6783. ETH-Zurich, 1981.
15. Grigg, H., *in* "The Porphyrins" (D. Dolphin, Ed.), Vol 2, Chap. 10. Academic Press, New York, 1978.
16. Johnson, A. W., *in* "Porphyrins and Metalloporphyrins" (K. M. Smith, Ed.), Chap. 18. Elsevier, Amsterdam, 1975.
17. Rasetti, V., "Synthesis of Nickel(II)-$\Delta^{18,19}$-dehydrocorrinates and Isobacteriochlorins," Ph.D. thesis, p. 77. ETH-Zurich, 1979.
18. Johansen, J. E., Piermattie, V., Angst, C., Diener, E., Kratky, C., and Eschenmoser, A., *Angew. Chem. Int. Ed. Engl.* **20,** 261 (1981).
19. Ofner, S., "Synthesis of Isobacteriochlorins and of C,D-Tetradehydrocorrins," Ph.D. thesis, Diss. ETH No. 6939. ETH-Zurich, 1981.
20. Burger, H., *in* "Porphyrins and Metalloporphyrins" (K. M. Smith, Ed.), Chap. 11. Elsevier, Amsterdam, 1975.
21. Buchler, J. W., *in* "Porphyrins and Metalloporphyrins" (K. M. Smith, Ed.), Chap. 5, p. 205. Elsevier, Amsterdam, 1975.

22. Angst, C., Kratky, C., and Eschenmoser, A., *Angew. Chem. Int. Ed. Engl.* **20,** 263 (1981).
23. Wei, J., and Prater, C. D., "Advances in Catalysis," Vol. 13, p. 203. Academic Press, New York, 1962.
24. Ware, R. A., and Wei, J., *J. Catal.*, **93,** 122 (1985).
25. Morales, A., and Galiasso, R., *Fuel* **61,** 13 (1982).
26. Worthington, P., Hambright, P., Williams, R. F. X., Reid, J., Burnham, C., Shamim, A., Turay, J., Bell, D. M., Kirkland, R., Little, R. G., Datta-Gupta, N., and Eisner, U., *J. Inorg. Biochem.* **12,** 281 (1980).
27. Hambright, P., personal communication, 1982.
28. Fuhrhop, J. H., and Subramanian, J., *Philos. Trans. R. Soc. London Ser. B* **273,** 335 (1976).
29. Scheer, H., and Inhoffen, H. H., *in* "The Porphyrins" (D. Dolphin, Ed.), Vol. 2, Chap. 2. Academic Press, New York, 1978.
30. Fuhrhop, J. H., *in* "The Porphyrins" (D. Dolphin, Ed.), Vol. 2, Chap. 5. Academic Press, New York, 1978.
31. Kwart, H., Schuit, G. C. A., and Gates, B. C., *J. Catal.* **61,** 128 (1980).
32. Subramanian, J., and Fuhrhop, J. H., *in* "The Porphyrins" (D. Dolphin, Ed.), Vol. 2, Chap. 8. Academic Press, New York, 1978.
33. Alder, R. W., Baker, R., and Brown, J. M., "Mechanism in Organic Chemistry," Chap. 2. Wiley, New York, 1971.
34. Sato, M., Takayama, N., Kurita, S., and Kwan, T., *Nippon Kagaku Zasshi* **92,** 834 (1971).
35. Todo, N., Kabe, T., Ogawa, K., Kurita, M., Sato, T., Shimada, K., Kuriki, Y., Oshima, T., Takematsu, T., and Kotera, Y., *Kogyo Kagaku Zasshi* **74,** 563 (1971).
36. Wei, J., *J. Catal.* **1,** 526, 538 (1962).
37. Spry, J. C., and Sawyer, W. H., Paper presented at 68th Annual AIChE Meeting. Los Angeles, November 1975.